Density, sp^3 fraction, and cross-sectional structure of amorphous carbon films determined by x-ray reflectivity and electron energy-loss spectroscopy

A. C. Ferrari,[1,*] A. Libassi,[2] B. K. Tanner,[2] V. Stolojan,[3] J. Yuan,[1,3] L. M. Brown,[3] S. E. Rodil,[1] B. Kleinsorge,[1] and J. Robertson[1]

[1]*Department of Engineering, University of Cambridge, Cambridge, CB2 1PZ United Kingdom*
[2]*Department of Physics, University of Durham, Durham, DH1 3LE United Kingdom*
[3]*Cavendish Laboratory, University of Cambridge, Cambridge, CB3 OHE United Kingdom*

(Received 1 June 2000)

Grazing-angle x-ray reflectivity (XRR) is described as an efficient, nondestructive, parameter-free means to measure the mass density of various types of amorphous carbon films down to the nanometer thickness range. It is shown how XRR can also detect layering if it is present in the films, in which case the reflectivity profile must be modeled to derive the density. The mass density can also be derived from the valence electron density via the plasmon energy, which is measured by electron energy-loss spectroscopy (EELS). We formally define an interband effective electron mass m^*, which accounts for the finite band gap. Comparison of XRR and EELS densities allows us to fit an average $m^*=0.87m$ for carbon systems, m being the free-electron mass. We show that, within the Drude-Lorentz model of the optical spectrum, $m^*=[1-n(0)^{-2}]m$, where $n(0)$ is the refractive index at zero optical frequency. The fraction of sp^2 bonding is derived from the carbon *K*-edge EELS spectrum, and it is shown how a choice of ''magic'' incidence and collection angles in the scanning transmission electron microscope can give sp^2 fraction values that are independent of sample orientation or anisotropy. We thus give a general relationship between mass density and sp^3 content for carbon films.

I. INTRODUCTION

The sp^3 fraction, the clustering of the sp^2 phase, and hydrogen and nitrogen content are the key structural parameters that determine the properties of amorphous carbons. Electron energy-loss spectroscopy (EELS) is currently the preferred method to obtain the sp^3 content from the size of the π^* peak in the carbon *K*-edge absorption spectrum. The low-energy-loss spectrum gives the valence plasmon energy and thereby the mass density, which is closely related to the sp^3 fraction. EELS has been widely used to study the bonding in many carbon systems such as conducting polymers, fullerenes, nanotubes, diamond, and disordered carbons.[1–10] EELS has also been used to probe the cross-sectional structure of diamondlike carbon (DLC) films.[11] However, EELS is a destructive and time-consuming method. EELS also requires a choice of an electron ''effective mass'' to derive the mass density from the plasmon energy.[12]

Grazing-incidence x-ray reflectivity (XRR) is a widely used nondestructive method to determine the structure of thin films and particularly of multilayered films.[13–18] It can be used on all different kinds of amorphous carbon thin films to obtain information on density, roughness, and cross-sectional layering without any sample preparation or damage.[19] From the measurement of the critical angle for total external reflection, the total electron density can be measured, from which the mass density can be derived directly. XRR also gives information on layering, without the complex sample preparation needed for cross-sectional EELS.

XRR has previously been used to study pure and hydrogenated carbon films,[20–28] generally to measure their density. Lucas, Nguyen, and Kortright[22] used XRR to follow the density changes due to the annealing of sputtered amorphous carbon (a-C) films. Martinez-Miranda *et al.*[28] used XRR to follow the density evolution during annealing of highly sp^3-bonded tetrahedral amorphous carbon (ta-C) films. Findeisen *et al.*[24] combined neutron and x-ray reflectivity to determine both the density and the H content of hydrogenated amorphous carbon (a-C:H) films. Logothetidis and Stergioudis[21] studied the relationship between roughness and thickness in sputtered a-C. Zhang *et al.*[27] made a thorough investigation of the effects of bias voltage and deposition pressure on a-C:H. Lucas, Nguyen, and Kortright[22] first reported a multilayer structure for dc magnetron sputtered a-C. Martinez-Miranda *et al.*[28] suggested the presence of a multilayer structure in ta-C grown by pulsed laser deposition (PLD), which was confirmed by using a combination of high-resolution transmission electron microscopy (TEM), Rutherford backscattering (RBS), and XRR.[29]

Four methods are mainly used to determine the mass density of carbon films: flotation, weight gain, RBS, and the EELS plasmon energy. The density values from each method generally agree for denser materials such as ta-C,[30] even though with broad data scattering.[10,32,33] However, weight gain gives lower values than flotation and plasmon energy for porous materials because the latter measure the microscopic density.[33] RBS is usually combined with profilometry, resulting in wide error bars. The derivation of density from the plasmon energy requires a choice of an electron effective mass. However, due to the lack of a precise definition of such an effective mass, different masses have been used by various groups,[10,32–34] resulting in different densities for the same plasmon energies.

In this paper we give a procedure to collect and analyze plasmon-energy data, and we formally define an interband effective electron mass, which is linked to the electronic band structure. XRR and EELS both probe the electron density of thin films; XRR the total electron density and EELS the valence electron density, so the combination of XRR and

0163-1829/2000/62(16)/11089(15)/$15.00 PRB 62 ©2000 The American Physical Society

TABLE I. Density, cross sectional structure, roughness (from XRR) and sp^3 content (from EELS) for different sets of films analyzed in this paper. In the density column we report the density of the thickest layer, for layered films. Details on interface and surface layer densities and thickness are reported in the third column, if good simulations could be achieved.

Sample	Density (g/cm^3)	Thickness (nm) and layering	Roughness (±1 Å)	sp^3 content (%)
ta-C single-bend FCVA −290 V	2.86±0.02 (bulk)	Layered	7	76
ta-C single-bend FCVA −250 V	3.12±0.02 (bulk)	64 (bulk)+4 (surf. 2.3 g/cm^3)	10	
ta-C single-bend FCVA −200 V	3.03±0.02 (bulk)	Layered (Fig. 4)	6	81
ta-C single-bend FCVA −80 V	3.24±0.02 (bulk)	63.5 bulk+7 (surf. 2.7 g/cm^3), Fig. 3	6.5	87
ta-C single-bend FCVA floating	2.91±0.02 (bulk)	Layered	8	78
ta-C single-bend FCVA +10 V	2.71±0.02 (bulk)	27.5 (interface, 2.56 g/cm^3)+37(bulk)+9(surf., 2.43 g/cm^3), Fig. 4	5	73
ta-C S-bend FCVA −300 V	3.17±0.03	70 (bulk)+2 (surf. 1.7 g/cm^3)	4	85
ta-C S-bend FCVA −100 V	3.26±0.03	76, Fig. 3	8	88
ta-C S-bend FCVA −20 V	3.13±0.03	84	7	86
ta-C PLD 9 J/cm^2	2.88±0.02 (bulk)	6 (interface 2.47 g/cm^3)+58.5 (bulk)+30.5 (surf., 2.74 g/cm^3), Fig. 4	8	
ta-C PLD 20 J/cm^2	3.0±0.02 (bulk)	Layered		
ta-C:N FCVA+ECWR (14% N)	2.75 (bulk)	5 (interface 2.4 g/cm^3)+27.5(bulk)+2(surf, 2 g/cm^3), Fig. 3b	6	64
ta-C:N FCVA+ECWR (20% N)	2.53 (bulk)	3 (interface 2 g/cm^3)+29.5nm(bulk)+2(surf., 1.75 g/cm^3)	6	57
ta-C:H ECWR (25% H)	2.39±0.03	82		70
ta-C:H ECWR (30% H)	2.13±0.03	95.5, Fig. 3	5.5	70
ta-C:H PBS (40% H)	1.6±0.035			65
ta-C:H:N ECWR (29% H, 16% N)	1.94±0.03	78.5(bulk)+1.5(surf.), Fig. 3	6	
a-C:H PECVD diamondlike	1.63±0.035	240, Fig. 2	5	58
a-C:H PECVD polymeric	1.3±0.04 (bulk)	255 (bulk)+6 (surf. 0.9 g/cm^3), Fig. 2.3		
a-C magnetron sputtering	1.72±0.035	Layered, Fig. 2.3	5	<20
a-C cluster assembled	0.9–1.4	⋯	⋯	~10

EELS allows a direct estimate of the effective mass. Indeed, we could fit a unique average effective mass for all *a*-Cs and diamond and thereby a general relation between density and coordination for carbons.

XRR is also a powerful tool to probe the cross-sectional layering of films. Analyzing a variety of films grown in different conditions, we find that extremely uniform or layered films can result from the same deposition system.

We also review the effects of probe convergence on the core-level electron energy loss of uniaxial materials, showing its implications for graphite and extending it to analyze the sp^2 phase in amorphous carbon films. We show how a choice of the convergence and collection angle will minimize anisotropy effects.[35,36] We thus find the optimum conditions to estimate the sp^3 fraction of *a*-C films.[8] We then discuss the residual effects of anisotropy of the sp^2 bond on the loss spectrum of amorphous carbon films, even if composed of an isotropic random distribution of sp^2 bonds.

II. EXPERIMENT

A. Samples

We analyzed different types of carbon films: *ta*-C, hydrogenated *ta*-C (*ta*-C:H), nitrogen-containing *ta*-C and *ta*-C:H, *a*-C:H, and sputtered *a*-C, together with nanostructured *a*-C formed by cluster-beam deposition (Table I). All samples were deposted on Si substrates. DLC is defined as an amorphous carbon film containing a sizable fraction of sp^3 bonding. The properties of DLC depend primarily on the mean ion energy used for deposition. Five sets of *ta*-C films were analyzed. The first set was deposited on a single-bend filtered cathodic vacuum arc (FCVA) system[10] with different bias voltages of −290, −200, and −80 V, the floating potential, and +10 V. The ion energy can be estimated by the magnitude of the bias voltage plus the plasma self-energy of ~10–20 eV. A second series of *ta*-C films was deposited at −20, −100, and −300 V on an S-bend FCVA.[37] A third series of *ta*-C films was deposited using a single-bend FCVA at a fixed bias voltage of −80 V with increasing deposition times (20, 30, 45, 60, and 90 s). A fourth series of *ta*-C was deposited with a floating potential with increasing deposition times (25, 50, and 75 s) using the defocused beam of an S-bend FCVA to achieve a very low deposition rate and thus ultrathin films. The fifth series was deposited by PLD at a laser fluence of 1, 9, 20, and 31 J/cm^2.[38] In PLD, *ta*-C properties depend on the laser fluence, which controls the effective ion energy, which increases with fluence.[38]

Three series of *ta*-C:H films were obtained from different electron cyclotron wave resonance (ECWR) sources (one slightly capacitively coupled) with an acetylene plasma and

an ion energy ranging from 80 to 170 eV.[39] These *ta*-C:H films contained approximately 30 at. % H, according to elastic recoil detection analysis (ERDA).[39] The third series consisted of two ultrathin *ta*-C:H films. One *ta*-C:H film was deposited from methane with a plasma beam source,[40] and ERDA gave a hydrogen content of ~40 at. %. Three *ta*-C:H:N films were deposited by an ECWR source from N_2/C_2H_2 gas mixtures. Their composition is known from a combination of ERDA and x-ray photoemission spectroscopy (XPS).[41] Two *ta*-C:N films were deposited by a combination of a carbon plasma from a FCVA and a nitrogen plasma from an ECWR.[42] Three *a*-C:H films were deposited from methane using a plasma enhanced chemical vapor deposition (PECVD) reactor: two of them with an estimated H content ~30 at. %, and one polymeric with an estimated H content of ~40–50 at. %. One *a*-C sample was deposited by dc magnetron sputtering.[43] Two nanostructured *a*-C films were produced by a carbon-cluster-beam source, using beams of different average cluster size.[44] This range of films is wider than covered by previous groups.

B. X-ray reflectivity

The refractive index of x rays in solids is slightly less than unity, so external reflection occurs at low angles of incidence. As the grazing-incidence angle θ_i increases above a critical angle θ_c, x rays start to penetrate the film. XRR measures the intensity reflected in the specular direction ($\theta_i = \theta_r$) as a function of the grazing-incidence angle.

The XRR curves were measured on a Bede Scientific GIXR reflectometer, with a Bede EDRa scintillation detector. The source was a copper target x-ray tube operated at 40 kV and 40 mA, monochromatized to the Cu K_β ($\lambda = 1.3926$ Å). The specular reflectivity curves were taken as a function of incidence angle using a θ–2θ scan, with the detector stepped at twice the step of the specimen. Specular and off-specular reflectivity curves were measured for each sample, with θ_i varying in the range $0''-8000''$, with a step of $20''$. An $0.1°$ offset of the sample angle was used for the off-specular measurements. The true specular reflectivity curves were obtained by subtracting the off-specular from the specular measurement to remove the forward diffuse scatter.

XRR probes a macroscopic area of sample. The x-ray beam width is 1–5 mm, while the beam is 100 μm high. At very small angles of incidence, the footprint on the sample is 1–5 mm by 1–2 cm. This is particularly significant when comparing roughness from XRR to atomic force microscopy (AFM) or scanning tunneling microscopy (STM), where the area probed is typically only 0.1–1 μm^2. The XRR curves of laterally inhomogeneous films are a convolution of different periods (i.e., the fringes are less marked). XRR provides an average characterization for films containing inhomogeneous regions. A typical case is the presence of heterogeneous macroparticles randomly distributed in the film: an average density is found, but no extra layering is evidenced.

Data were extracted by fitting to the experimental curve a simulated reflectivity curve using the Bede REFS-MERCURY software package. This uses Parrat's recursive formalism of the Fresnel equations to calculate the reflected wave amplitude and thus the reflected intensity.[13–17] A genetic algorithm is used to minimize the logarithm of the difference in the absolute intensity between the simulated and experimental curve, as the model parameters are adjusted by the computer. Atomic scale roughness causes x rays to be scattered from the specular beam, giving rise to a weaker specular reflected beam. Thus the intensity falls faster than the $(2\theta)^{-4}$ law of a perfectly smooth surface. By combining specular and diffuse scatter, genuine surface roughness can be separated from compositional grading (i.e., smooth variations of density along the direction normal to the interface), which also results in a rate of fall faster than $(2\theta)^{-4}$.[15] Surface and interface roughnesses were incorporated within the distorted-wave Born approximation using a Gaussian variation of the electron density gradient, to get rms roughnesses. The Born wave approximation models the attenuation of the specular scatter, caused by the presence of roughness at the interface, with the inclusion of a Debye-Waller factor

$$I_{\mathrm{spec}} = I_0 \exp(-q_z^2 \sigma^2), \tag{1}$$

where q_z is the component of the scattering vector normal to the film and σ is the rms roughness. From conservation of energy, the diffuse intensity can be expressed as

$$I_{\mathrm{diff}} = I_0 - I_{\mathrm{spec}} = I_0 [1 - \exp(-q_z^2 \sigma^2)]. \tag{2}$$

The ratio of the integrated diffuse intensity to the integrated specular intensity therefore depends only on the scattering vector and the roughness of the interface:[45]

$$\frac{I_{\mathrm{diff}}}{I_{\mathrm{spec}}} = \exp(q_z^2 \sigma^2) - 1. \tag{3}$$

Thus the surface roughness is deduced by measuring the integrated intensity of the diffuse and specular scatter in a transverse scan in which the detector angle (and q_z) is fixed and the detector scans through the specular condition. This method assumes that all diffuse scatter is accessible. This is not true in general and may underestimate the roughness.[18] For multiple interfaces,[45] it is still possible to obtain estimates of the roughness, if the interface roughness is uncorrelated (as here) from one interface to the other. The value obtained is an average from all the interfaces. Simulations show that in our films this method is sensitive mainly to the surface roughness, due to the small differences in electron density across internal surfaces. Macroparticles eventually present on the surface do not influence the roughness determination if their size is larger than the x-ray coherence length.

C. Electron energy-loss spectroscopy

The EELS measurements were carried out on a VG 501 scanning transmission electron microscope (STEM) equipped with a dedicated spectrometer with a McMullan parallel EELS detection system. The samples were prepared for microscopy by removing the Si substrates with a $HF:HNO_3:H_2O$ (1:8:4) etching solution and placing film segments on Cu grids.[10] 40 carbon *K*-edge spectra were collected for each sample, as well as the low-loss spectrum containing the plasmon and the zero-loss electrons. Both spectra were deconvoluted by the Fourier logarithm ratio with the spectra of the electron beam passing through

vacuum.[46] The background was then removed from the carbon K edges, followed by the removal of multiple scattering by deconvolution with the low-loss spectrum by the Stephens method.[46] The π^* peak at 285 eV of the carbon K edge was fitted by a Gaussian, and its area was normalized to the area of the σ^* edge in the window 284–310 eV, following Berger, McKenzie, and Martin.[9] The sp^2 content is obtained by referencing this ratio to its value for graphite as described in Sec. III D.[9,10] The plasmon energy is derived by fitting the energy-loss function to the single plasmon peak, as described in Sec. III E.

All spectra are collected at a convergence angle of 7.4 mrad and an acceptance angle of 7 mrad, for 100-keV electrons. This ensures that all sample directions are equally probed at the K-edge energy, so the results should be independent of any anisotropy in the films (see Sec. III D).[35]

III. RESULTS AND DISCUSSION

A. XRR theory

The x-ray refractive index of a material with elements j of atomic number Z_j, molar masses M_j, density ρ_j is given by[14]

$$n=1-\frac{N_A}{2\pi}r_0\lambda^2\sum_j \frac{\rho_j}{M_j}f_j, \tag{4}$$

where $r_0=e^2/4\pi\varepsilon_0 mc^2$ is the classical electron radius, m is the electron mass, and N_A is the Avogadro number. The parameter

$$f_j=Z_j+f_j'+if_j'' \tag{5}$$

includes dispersive and absorptive corrections, which are only significant near an absorption edge. Thus n can be written as

$$n=1-\delta-i\beta, \tag{6}$$

with

$$\delta=\frac{r_0\lambda^2}{2}\sum_j \frac{\rho_j}{M_j}(Z_j+f_j'), \tag{7}$$

$$\beta=\frac{N_A}{2\pi}r_0\lambda^2\sum_j \frac{\rho_j}{M_j}f_j''=\mu\frac{\lambda}{4\pi}, \tag{8}$$

where μ is the linear absorption coefficient in cm^{-1}, given by the product of the mass attenuation coefficient and the density. $\mu\sim 3\rho$ for carbon at $\lambda=1.3926$ Å.[47]

Applying Snell's law at the air/film interface gives the critical angle

$$\theta_c=\sqrt{2\delta}=\lambda\sqrt{\frac{N_A r_0}{\pi}\sum_j \frac{\rho_j}{M_j}(Z_j+f_j')}. \tag{9}$$

θ_c is usually very small, e.g., at $\lambda=1.3926$ Å it is 0.201° for Si and 0.245° for diamond. It is useful to consider three elements in our films, carbon, hydrogen, and nitrogen, so

$$\theta_c=\lambda\sqrt{\frac{N_A r_0}{\pi}\rho\frac{X_C(Z_C+f_C')+X_H(Z_H+f_H')+X_N(Z_N+f_N')}{X_C M_C+X_H M_H+X_N M_N}}, \tag{10}$$

where ρ is the overall mass density and X_j is the atomic fraction of element j. At $\lambda=1.3926$ Å, $f_j'\sim 10^{-2}$,[47] so we take $f_j'=0$ and obtain, with $X_H=1-X_C-X_N$:

$$\rho=\frac{\pi^2c^2\varepsilon_0}{3\lambda^2N_Ae^2}M_C m\theta_c^2\frac{11X_C+13X_N+1}{5X_C+6X_N+1}. \tag{11}$$

Note that the dependence on the H content is quite weak in the usual range $X_H=10$–50% (e.g., $\rho=2.3\,\mathrm{g/cm^3}$ if $X_H=0.1$ and 2.16 g/cm^3 if $X_H=0.5$, with $X_N=0$, $\theta_c=720''$, and $\lambda=1.3926$ Å).

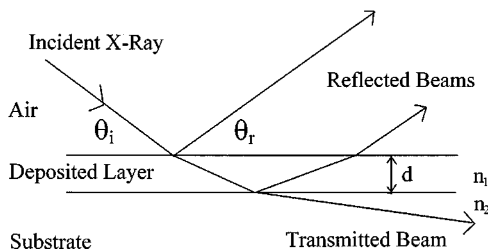

FIG. 1. Specular reflection of x rays under grazing incidence from a single layer of refractive index n_1 and thickness d on a substrate of refractive index n_2. θ_i is the grazing-incidence angle; θ_r is the reflectance angle. For a typical $\theta_i=5$–10 mrad, given the beam cross-section perpendicular to the specimen of ~100 μm and a width of 1–5 mm, the footprint on the sample is ~1–5 mm ×1–2 cm. Note that in the XRR profiles the increase in the reflected intensity before the critical angle is related to the size of the sample with respect to the variable beam footprint at small angles of incidence. The simulation software takes this into account.

For a thin layer deposited on a substrate (Fig. 1), the two reflected rays can interfere and, from Snell's law, constructive interference occurs when

$$\theta_i^2=\theta_c^2+\frac{\lambda^2}{4d^2}(k+1/2)^2 \quad \text{when } n_1<n_2, \tag{12}$$

$$\theta_i^2=\theta_c^2+\frac{\lambda^2}{4d^2}k^2 \quad \text{when } n_1<n_2, \tag{13}$$

respectively, where d is the thickness and k is an integer. For $\theta_i>2\theta_c$ the fringe period gives $\Delta\theta\approx\lambda/2d$, so the thickness is found from the fringe period. This formalism has been extended by Parrat to treat multiple interfaces and multilayers.[13]

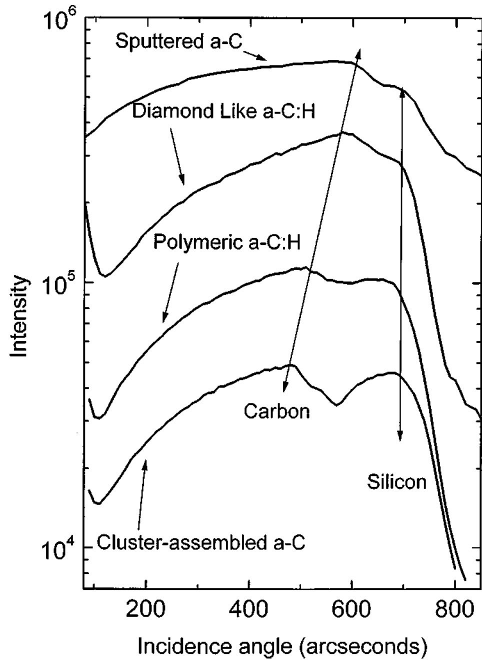

FIG. 2. X-ray specular reflectivity profile for sputtered a-C, diamondlike a-C:H, polymeric a-C:H and cluster-assembled films. Their electron density is lower than the silicon substrate, so they show a double critical angle, as indicated.

B. XRR results

Some films such as ta-C:H have a density similar to or just less than Si (2.33 g/cm^3). Thus the observed critical angle is the Si critical angle and not that of the film. The film only perturbs the shape of the critical angle and the reflectivity curve must be simulated to extract the film density. For less dense films such as cluster-assembled carbon films, a-C:H or a-C, a double critical angle is seen, allowing a better determination of the density. If the film density is less than the substrate, x rays first penetrate the film, when the incidence angle exceeds the film critical angle, and the reflectivity falls sharply due to absorption in the film, until they are totally externally reflected at the film-substrate interface. When the incidence angle exceeds the larger substrate critical angle, x rays penetrate the substrate and the reflectivity falls further, as in Fig. 2.

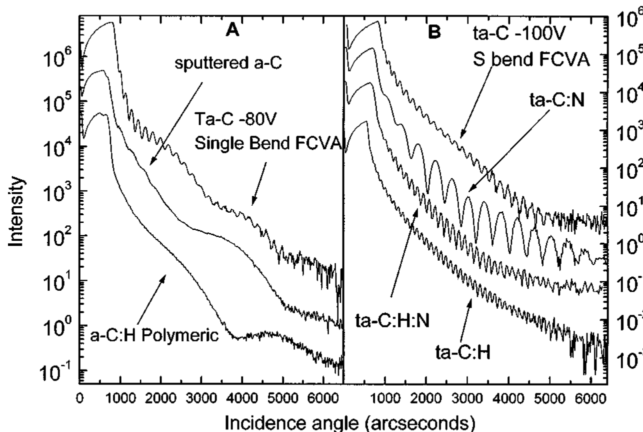

FIG. 3. Representative x-ray reflectivity profiles from various films: a-C, a-C:H, ta-C:H, ta-C:H:N, ta-C, and ta-C:N. (A) Layered films; (B) uniform films.

Figure 3(b) shows a typical XRR curve for a ta-C:H film. There is only one fringe period, i.e., there is a single layer. The fringe period gives the film thickness directly. Very good simulations of the measured curves were obtained for these films, including a 1–2 nm layer of different density at the film-substrate interface [possibly composed of Si, C, and O (Refs. 22 and 11)] and sometimes a ~1 nm layer at the surface. ta-C:H films from the more capacitively coupled ECWR have a density of 2.3–2.4 g/cm^3, while the others have densities in the range 2.1–2.23 g/cm^3 (Table I). A similar behavior was found for ta-C:H:N films (Table I), Fig. 3(b). These films were 80–100-nm thick.

Similar results were obtained for a-C:H, with the main difference of a clear double critical angle. We find a density of 1.64–1.74 g/cm^3 for the diamondlike a-C:H and 1.3 g/cm^3 for the polymeric a-C:H [Figs. 2 and 3(a)]. The simulation of the latter film required two layers of 3.5 and 5.8 nm of lower density (0.85 and 0.87 g/cm^3) at the Si/C and C/air interface. These a-C:H films were 160–240-nm thick.

The magnetron sputtered a-C film shows a clear double critical angle, corresponding to a density of 1.7 g/cm^3, Fig. 2. Figure 3(a) shows three different fringe periods, corresponding to 360 nm (total thickness) and 40 and 5 nm (surface layers), with a density of the surface layers varying between 1.7 and 1.15 g/cm^3.

A clear double critical angle is seen for the nanostructured a-C films, Fig. 2. The density varies from 0.8 to 1.4 g/cm^3 accordingly with the cluster size during deposition. Films grown with smaller clusters have higher density.[44]

For ta-C films, there is a single critical angle from the film, as its density is larger than the substrate. The error on density is less than for hydrogenated films (Table I). Densities up to 3.26 g/cm^3 were obtained for an ~88% sp^3 film grown on the S-bend FCVA.

The reflectivity curves of some ta-C films grown on the single-bend FCVA show fringes with multiple periodicities, indicating the presence of a significant layering, not just 1–2 nm at the surface or interface.[29] If a film consists of a dense bulk layer, with a less dense top and a bottom layer, the critical angle (and thus the resulting density) is that of the bulk layer. Thus, in general, we obtain the critical angle and density of the densest layer, and not the average film density, which requires a fit of the multilayer structure.

In more detail, the penetration depth for incidence above the critical angle is[48,49,29]

$$D=\frac{\lambda}{2\pi q}, \tag{14}$$

where

$$q=\sqrt{\frac{(\theta_c^2-\theta_i^2)+\sqrt{\theta_c^2-\theta_i^2)^2+4\beta^2}}{2}}, \tag{15}$$

and β is defined in Eq. (8). From Eqs. (14), (15), and (8), the penetration depth at the critical angle, D_c, as a function of carbon mass density and absorption coefficient, is

$$D_c=\sqrt{\frac{\lambda}{\pi\mu}}, \tag{16}$$

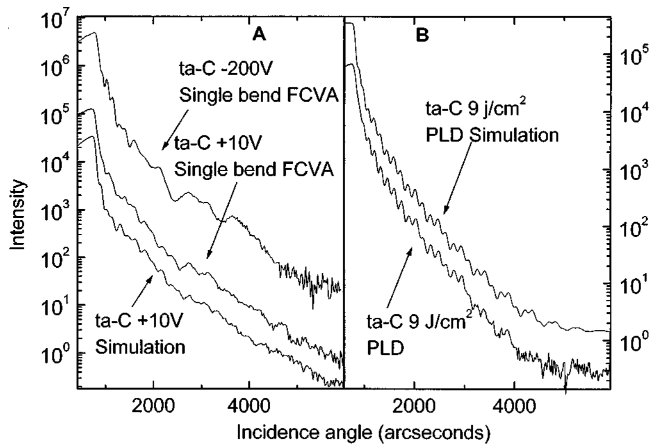

FIG. 4. X-ray reflectivity profiles from heavily layered FCVA and PLD *ta*-C films. (A) also compares the simulated XRR curve of a single-bend *ta*-C grown at +10 V with the measured one; (B) compares the measured and simulated curve for a PLD *ta*-C. The structure resulting from the simulations is reported in Table I.

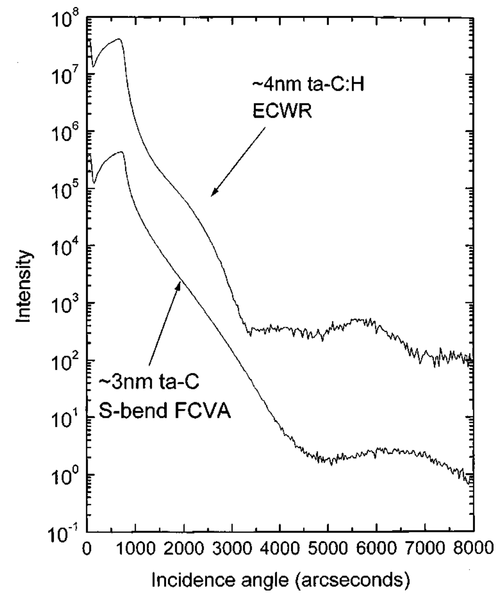

FIG. 5. X-ray reflectivity profiles from ultrathin *ta*-C and *ta*-C:H films, the nominal thickness is also indicated. The structure resulting from simulations is reported in Table II.

so $D_c \sim 385[\rho(\mathrm{g/cm^3})]^{-0.5}$ nm for carbon at $\lambda = 1.3926$ Å.[47]

At θ_c x rays start to penetrate and the rapid fall in intensity defines the critical angle. D_c is smaller for larger densities. For a density ~ 3 g/cm^3 D_c is $\sim$200–250 nm. If the surface layer is thicker than D_c, we would directly see, in the specular scan, the critical angle corresponding to the density of the first D_c nanometers of this surface layer. In our case, the surface layer is usually less than 10 nm and so the x rays penetrate without giving a ''surface'' critical angle. We thus directly see the density of the bulk layer (of its upper part, limited by the penetration depth at this density). If the surface region has a density gradient, or if the distinction between the bulk and the surface layer is not sharp, the critical angle may be less well defined and may refer to an average density of a surface region whose thickness is defined by the penetration depth. Thus, for layered films, the reflectivity curve must be simulated to get densities of the other layers and thus the average density. Note that our definition of D_c gives values $\sim$5 times bigger than D_c derived by Siegal *et al.*,[29] but in agreement with critical angles obtained from simulations of structures composed of high- and low-density layers of various thicknesses. This difference stems from a different definition of the characteristic penetration depth at the critical angle, given the large gradient of D around θ_c. However, Eq. (16) accounts better for the measured critical angles.

Figure 3(a) shows the reflectivity curve of a single-bend FCVA film grown at −80 V bias. We can see a short period due to the overall film thickness and a long period due to a less dense 7 nm surface layer. Other films have more complex curves; see Fig. 4. The number of layers and their density, thickness, and roughness all vary, and the density of the top and bottom layers (and possibly of bulk) is probably not constant (e.g., the interfaces are not sharp), while the sp^3 content does not vary so much with bias (Table I). Simulation of such structures is difficult.

Figure 4(a) shows a simulation in which a three-layer model gives a reasonable account of the measured reflectivity of the *ta*-C film grown at +10 V. The sharp uniform layer approach failed for the first series of single-bend FCVA films grown at higher energies, as the density is not constant in each layer. The total film thickness of these films is 50–70 nm. XRR alone cannot fully describe such complex films. Combining XRR and cross-sectional HRTEM could give a better starting point for fitting reflectivity curves, leading to a better determination of the density of the single layers. An estimate of the average film density can be obtained from EELS (see Sec. III E). The different cross-sectional structure of this first series of *ta*-C films was confirmed by Siegal *et al.*[29] through HRTEM. Single-bend FCVA films at −80 V have always been considered ideal films, having the highest density and sp^3 content.[10] These results would also suggest that they are also the most uniform, with the thickest bulk layer and thinnest interfaces. We found similar layered structures for PLD *ta*-C films; see Fig. 4(b). Layering in PLD *ta*-C was found also by Siegal *et al.*[29] They also reported the presence of a Bragg scattering peak attributed to quasiperiodical nanometer-sized regions of localized strain fields. However, we never detected such a peak in our films, irrespective of the deposition system.

In contrast, films grown on the S-bend FCVA show much higher uniformity and only weak dependence of density and layering on the substrate bias (Table I). Surface layers never exceed 1–2 nm. The thickest one, 2 nm, is on a film grown at −300 V bias. The largest bulk density is 3.26 g/cm^3, corresponding to $\sim$88% sp^3 content. The high uniformity in these films was confirmed by Brillouin scattering, as an optimum fit of the experimental data was obtained with a single layer film.[50] In contrast, Brillouin data of the −80 V single-bend FCVA film could not be fitted by one layer.[50]

The top surface rms roughness is 5–8 Å for all films (Table I). The roughness of the nanostructured carbon film is too large [>10 nm (Ref. 44)] to be properly determined.

Figure 5 shows XRR data on ultrathin *ta*-C and *ta*-C:H films, indicating the ease of XRR to measure films in the nanometer range. In particular, the structure of the thinnest *ta*-C film, deposited at the floating potential, consisted of

TABLE II. Density, cross-sectional structure, and roughness from XRR for a series of *ta*-C films grown with a single-bend FCVA for increasing deposition times and for two series of ultrathin *ta*-C and *ta*-C:H films grown with the S-bend FCVA and the ECWR sources. The density column gives the density of the thickest layer. Details on the interface and surface layer densities and thickness are reported in the third column.

Increasing deposition time (s)	Density (cm^3)	Thickness (nm) and layering	Roughness (±1 Å)
ta-C single bend FCVA −80 V			
20	3.20±0.02	2.3 (interface, 2.75 g/cm^3)+12.7 (bulk)	4.5
30	3.20±0.02	1.4 (interface, 2.35 g/cm^3)+25.2 (bulk)	5
45	3.20±0.02	2 (interface, 2.7 g/cm^3)+44 (bulk)	5.5
60	3.20±0.02	3.1 (interface, 2.6 g/cm^3)+57.8 (bulk)	9.5
90	3.20±0.02	2.2 (interface, 2.9 g/cm^3)+71.5 (bulk)	10
Ultrathin S-bend FCVA, floating pot., defocused beam			
25	3.05–3.10	0.5–0.8 (interface, 2–2.2 g/cm^3)+3–3.5 +0.5–0.8 (surf. 2–2.5g/cm^3), Fig. 5	<10
50	3−3.2	0.5–1.5 (interface, 2–2.2 g/cm^3)+4.5+0.5 (surf.)	8
75	3–3.2	1.5 (interface, 2.5 g/cm^3)+4.8 +1.7–1.8 (surf. 2.2–2.4 g/cm^3)	4
Ultrathin *ta*-C:H ECWR			
7	2.1	2–3(interface, 2–2.1 g/cm^3)+2.3–3.2 +2 (surf. 1.5 g/cm^3), Fig. 5	5

3–3.5 nm of 3.05–3.1 g/cm^3 density with a 0.5–0.8-nm surface layer of 2–2.5 g/cm^3 density and a 0.5–1-nm interface layer (Table II).

C. XRR discussion

These results show how XRR gives considerable information on density, roughness, thickness, and layering in a fast and nondestructive way. The *a*-C:H films consist mainly of a bulk layer, sometimes with very thin Si/C and C/air interfaces. The cross-sectional structure varies weakly with ion energy. Zhang *et al.*[27] reported an increase of surface and interface roughness (from 0.5 to 1.5 nm) and interface layer thickness (from 3 to 5 nm) for *a*-C:H deposited with increasing ion energy. In contrast, we found a difference in the cross-sectional nanostructure of the *ta*-C series grown with single-bend and double-bend FCVA. Furthermore, a significant surface layer is found in sputtered *a*-C grown at much lower ion energy than *ta*-C. Although ~1 nm thick layers are predicted by subplantation,[51,52] it is not possible to explain within this theory the development of such complicated structures as those shown in Fig. 4. Siegal *et al.*[29] proposed heavy layering as an intrinsic property of *ta*-C. However, we find that layering is just a by-product of plasma fluctuations during deposition and can thus be completely eliminated.

Indeed, our data clearly show that it is possible to grow very uniform *ta*-C and that heavy layering is not necessary but depends on deposition conditions. The S-bend and single-bend FCVA work on the same principle. The S-bend FCVA provides better filtering of the macroparticles.[37,53] There is no fundamental physical reason why one machine should produce uniform films and the other more layered ones. Siegal *et al.*[29] proposed that the formation of the bulk denser layer is due to backscattering of C atoms from the Si substrate, predicting a scaling of the interface layer with ion energy. However, this mechanism cannot explain why the layers are well over 1 nm thick, which is the range of C ions at the usual 10–400 eV deposition energies.[51] The range is clearly even smaller for C atoms backscattered at the Si substrate. This cannot also explain layers in sputtered *a*-C, grown at very low deposition energy. Siegal *et al.*[29] also proposed that the less dense surface layer should originate to counteract the stress energy resulting from the growth process. However, our layered and uniform *ta*-C films have comparable stresses of ~10 GPa, thus showing that no stress-releasing-induced layering is present. Note also that the structure of the ultrathin S-bend *ta*-C films resembles that of thicker S-bend films, with a scaling of the bulk layer, but not of the surface and interface ones (these are ~1 nm in both thick and thin films).

A hint of the origin of the layering comes by considering the plasma in a FCVA or an ECWR. An ECWR plasma can run with extreme stability for hours. A FCVA plasma is much less stable. The plasma lasts for 3–4 min and the cathode spot moves during the deposition, sometimes requiring repositioning in the center and restriking the plasma.[53] This causes plasma fluctuations. We first checked the possible influence of triggering of the arc during *ta*-C deposition, by producing a film in a single strike or in more than one strike. As reported before,[11] the structure is unchanged, suggesting that triggering itself has negligible effect on the growth process. However, plasma instabilities and transients in ion energy and current density during the deposition could be responsible for the layering. We thus produced a series of films with increasing deposition times, from 20 to 90 s at −80 V, using the single-bend FCVA. A new cathode was used and extreme care was taken to position the striker during the deposition. As shown in Table II, no surface layer was detected and only a ~2 nm interface layer was produced. The

rms roughness increased with thickness, reaching a maximum of ~1 nm. We then grew another film at −250 V; we still found a 4 nm-thick top layer, but layering was much less than in films previously grown at a similar bias. Furthermore, Davis, Knowles, and Amaratunga[11] analyzed samples prepared at −300 V with our single-bend FCVA by cross-sectional EELS and very uniform films were obtained (with 5-nm interface and 1-nm surface layers). McKenzie *et al.*[54] also reported layering in their FCVA *ta*-C films, which they attributed to plasma instabilities.

Further work has to be devoted to deeper investigate the relation between layering and plasma instabilities, and a feedback system should be required to minimize them. Here we just stress that heavy layering is not an intrinsic property of *ta*-C and that extremely uniform *ta*-C films can be grown at various bias voltages. There is no physical mechanism that can explain less dense layers of the order 10 nm at surface or interface if the ion energy and current densities are kept constant. Backscattering from Si could contribute only in the first 1–2 nm.

It is clear that a similar overall density and sp^3 content but different cross-sectional nanostructure could give different tribological, mechanical, electrical, and electronic behavior. This could explain the often contradictory behavior reported in literature. It is also clear that care should be taken whenever surface sensitive methods are compared to bulk methods.

D. EELS effect of anisotropy of the sp^2 bond on the sp^3 quantification in carbons

The sp^2 ratio is deduced from the electron energy-loss spectra by using the integrated intensity of the $1s$-π^* carbon pre-K edge, normalized to an energy window, and referred to an equivalent ratio for graphite, assumed to have 100% sp^2 bonding:[9]

$$sp^2=\frac{\left[\frac{\text{area}(\pi^*)}{\text{area}(\pi^*+\sigma^*)}\right]_{\text{sample}}}{\left[\frac{\text{area}(\pi^*)}{\text{area}(\pi^*+\sigma^*)}\right]_{100\%\ sp^2\ \text{reference}}}. \tag{17}$$

Core-loss spectra in a STEM are taken from very localized regions. A highly convergent beam is used for a focused probe and a large angular aperture is used to collect the maximum EELS signal. Thus the detected signal includes a range of momentum transfers at various orientations.

The effect of the convergent probe used in the STEM on the effective cross section of the inelastic excitation has been studied for isotropic materials[55,56] and quantified for uniaxial anisotropy by Browning, Yuan, and Brown[57] and Menon and Yuan.[35] For core-loss excitation we can assume $\varepsilon_1 \sim 1$ and $\varepsilon_2 \ll 1$, where ε_1 and ε_2 are the real and imaginary parts of the complex dielectric function ε. Thus $\text{Im}(1/\varepsilon)\approx\varepsilon_2$, so the response of the material under a time-varying electric field is given by ε_2. The imaginary part of the dielectric function can have different functional forms in different directions, such as in the case of a carbon atom with sp^2 hybridization, with uniaxial anisotropy. The angle integrated energy-loss cross section is then[35]

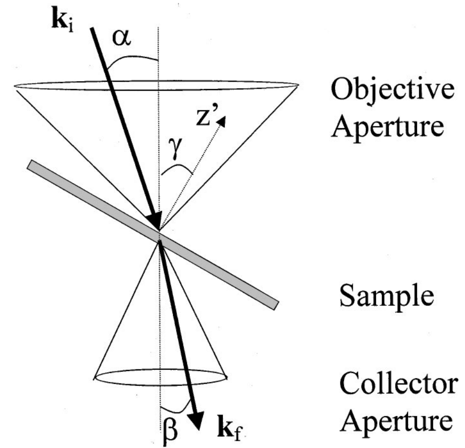

FIG. 6. Scattering geometry in electron energy-loss spectroscopy: $\mathbf{k}_i$ and $\mathbf{k}_f$ indicate the momentum of the incident and scattered electrons; γ is the angle between the local z axis (Z) and the incident beam; α and β are the convergence and collection semiangles.

$$\frac{d\sigma(\alpha,\beta,\gamma;E)}{dE}=[X(\alpha,\beta,\gamma;E)\varepsilon_2^{\perp}+Y(\alpha,\beta,\gamma;E)\varepsilon_2^{\parallel}]\pi\alpha^2, \tag{18}$$

where α and β are the convergence and collection semiangles as defined in Fig. 6 by the objective and collector apertures. γ is the angle between the local z axis (e.g., the π orbital at a sp^2 site) and the incident beam. E is the energy lost. $\varepsilon_2^{\perp}$ and $\varepsilon_2^{\parallel}$ are the components of the imaginary dielectric function perpendicular and parallel to the anisotropy axis. The weighting factors of the two components, X and Y, are the projection of the momentum transfer along the principal axis of the uniaxial crystal. X and Y can be factored in terms of the tilt angle γ as[35,36]

$$X(\alpha,\beta,\gamma;E)=\xi_0+\xi_1\cos^2\gamma+\xi_2\sin^2\gamma, \tag{19}$$

$$Y(\alpha,\beta,\gamma;E)=\xi_1\sin^2\gamma+\xi_2\cos^2\gamma, \tag{20}$$

where $\xi_i=\xi_i(\alpha,\beta,E)$ are aperture-dependent factors.

The first peak of the K edge is the $1s$ to π^* transition with momentum transfer $\Delta\mathbf{q}$ parallel to the z axis, and the next broad structure is related to $1s$ to σ^* transitions with $\Delta\mathbf{q}\perp z$, which superimpose on an atomic, hence isotropic, ionization absorption edge. The quantity needed for the π^* peak area is the parallel weighting fraction

$$Y'=Y/(X+Y). \tag{21}$$

This quantity is proportional to the probability of excitation parallel to the z axis of a sp^2 bond, after spectrum normalization. Substituting Eq. (21) in Eq. (18) and normalizing to the isotropic angular detection factor $Z=X+Y$, we can write the detected intensity $I(E)$ as

$$I(\alpha,\beta,\gamma;E)\propto[1-Y'(\alpha,\beta,\gamma;E)]\varepsilon_2^{\perp}+Y'(\alpha,\beta,\gamma;E)\varepsilon_2^{\parallel}. \tag{22}$$

Equation (22) shows that, as well as the obvious dependence of intensity on orientation γ, I also depends on the convergence and collection aperture angles. For example, in graphite, with the beam parallel to $z(\gamma=0)$, the set (0,7.2) mrad

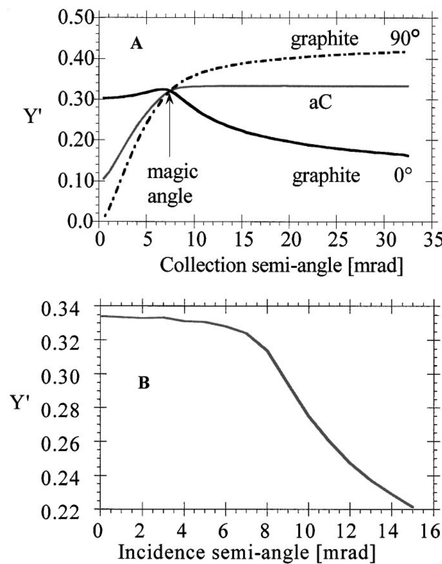

FIG. 7. (A) Calculated comparison of the variation of the weighting fraction Y' with collection semiangle β at incidence semiangle $\alpha=7.4$ mrad, for graphite (with $\gamma=0°$ and 90°) and an ideal isotropic 100% sp^2 a-C. (B) Calculated variation of the weighting fraction along the path of the magic angle (i.e., for a fixed α, the value of β is fixed).

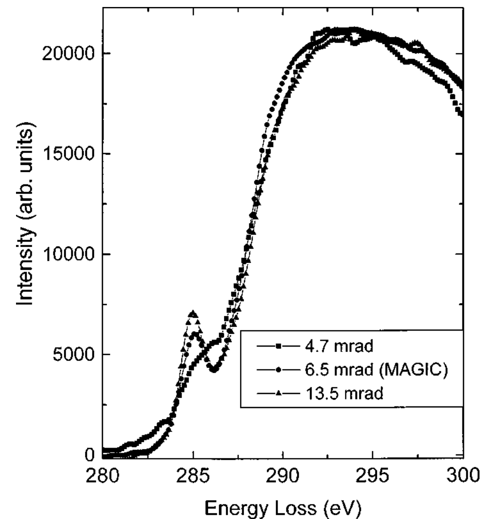

FIG. 8. K edge of ta-C at the magic collection angle (6.5 mrad) and at lower (4.7 mrad) and higher (13.5 mrad) collection angles.

and (7.4,2.6) mrad for (α,β) correspond to $Y'=0.897$ and 0.306, respectively, i.e., to a factor of 3 change in the $\pi^*/(\pi^*+\sigma^*)$ ratio.[35] Menon and Yuan[35] showed that there is a choice of (α;β) called the *magic angle* for which $\xi_1=\xi_2$, and thus, from Eqs. (19) and (20), X and Y become orientation independent. This means that at the magic angle we can spin a graphite crystal in the beam without any change of the normalized area of the π^* peak.[35]

In a truly amorphous material we expect a random orientation of sp^2 sites, so that Eq. (22) must be averaged over all orientations. However, this averaging does not eliminate the (α,β) dependence of the $\pi^*/(\pi^*+\sigma^*)$ ratio, although we expect much less change due to the random orientation of sp^2 bonds. The contribution to the spectra from each bond will be weighted according to its orientation γ. In the cylindrical coordinates defined by the beam, the average Y' for all the γ is[36]

$$\bar{Y}'=(\tfrac{1}{3}\xi_1+\tfrac{2}{3}\xi_2)/(\xi_0+\xi_1+\xi_2). \tag{23}$$

As $\xi_i=\xi_i(\alpha,\beta,E)$, it is clear that a residual dependence of $\bar{Y}'$ on the convergence and collection angles exists even for an isotropic distribution of sp^2 bonds. Thus the intensity of the K edge for the same a-C sample depends, in principle, on the particular experimental conditions.

The extra dependence of Eq. (22) on (α,β) can be exploited to find a particular (α,β) set for which I becomes independent of γ.[35] The magic (α,β) can be calculated for each element. For our VG501 STEM, the convergence angle at the objective aperture of 7.4 mrad needs a collection magic angle of 7 mrad. The closest to this optimum with our setup are (7.4, 6.5) mrad, respectively, corresponding to a 5% variation in the parallel weighting factor over a $\pi/2$ rotation of γ.[35]

Figure 7(a) compares the calculated variation of the weighting fraction with collection semiangle at an incidence semiangle of 7.4 mrad, for graphite (oriented parallel and perpendicular to the beam) and for an ideal isotropic 100% sp^2 amorphous carbon with an isotropic distribution of sp^2 bonds. Figure 7(a) clearly shows that the magic angle is the only situation in which the normalized area of the π^* peaks in the ideal a-C and graphite correspond 1:1. Away from this condition, the areas must be scaled by their respective weighting fractions to be compared. Figure 7(b) shows the calculated variation of the weighting fraction along the path of the magic angle (i.e., for each α, the corresponding β is calculated and fixed). This shows that the calibration at each magic angle is not equivalent, but the corrections become significant (>5%) only for incidence angles over ~7.5 mrad.

Berger, McKenzie, and Martin[9] proposed to use as a 100% sp^2 reference the graphite standards in the form of combined test specimen for electron microscopy averaged over a large area, where they are randomly distributed. Figure 7(a) shows that this standard is only slightly different from the magic-angle case. Alexandrou *et al.*[58] proposed to use C_{60} as a reference, which suffers from rapid beam damage under electron beam. It is clear that an alternative approach is to eliminate the orientation dependence completely using a graphite sample and working at the magic angle. On the other hand, working away from the magic angle gives big differences with respect to the optimal conditions, resulting in incorrect estimates of the sp^2 fraction. The error increases for a less isotropic distribution of the sp^2 sites. In fact, even if the reference and the sample are measured in the same conditions, the sp^2 values are correct only if they both have the same medium-range order.

Figure 8 shows a difference in the π^* intensity for a ta-C sample measured at the magic angle and at low collection angle. This demonstrates how the anisotropic nature of the sp^2 bond is detectable even in an a-C, which should have no preferential sp^2 orientation, as predicted by Fig. 7(a).

The most important consequence of the anisotropy analysis is that it opens the way to quantify orientation and medium-range order (within the probe size) for the sp^2 phase in carbon films and for anisotropic materials in general. Measurements can be taken at different collection

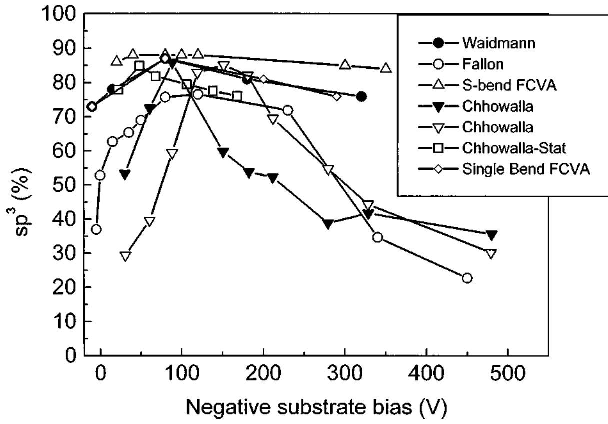

FIG. 9. sp^3 fraction as a function of negative bias voltage for ta-C films grown by our single-bend and S-bend FCVA's. Data on single-bend FCVA from Waidmann *et al.* (●) (Ref. 73), Fallon *et al.* (○) (Ref. 10), Chhowalla (Ref. 63) (▽, ▼; different coil current), Chhowalla stationary arc (Ref. 63) (□), and this work (◇). Data on S-bend FCVA from this work (△).

angles and the Y'-vs-β line can be experimentally determined. This line depends on the average γ of the sp^2 phase within the probe size and thus will allow a direct measurement of the average orientation of the sp^2 phase. K-edge measurements on fullerenes, nanotubes, and onions, with much more medium-range order than a-C will give lines in the (Y',β) space limited by the lines of graphite at $\gamma=0°$ and $\gamma=90°$. For those materials, (α,β) for the best TEM pictures are usually not the magic-angle (α,β) necessary for EELS. As an example, Fig. 8 also plots the K edge at 13.5 mrad, showing a slightly higher Y' with respect to the magic angle. This, according to Fig. 7(a), is an indication that the sp^2 phase even in as-deposited ta-C, where limited sp^2 clustering is present, cannot be completely randomly distributed, but shows a slight average preferential orientation of π bonds parallel to the substrate. A similar result was derived on another sample with on-axis and off-axis measurements.[59] We also applied this technique to study samples deposited at high temperature and annealed after deposition. We found that high-temperature deposition leads to increasing sp^2 cluster size with the average C axis parallel to the Si substrate. On the other hand, samples annealed after deposition show a preferential orientation with the C axis perpendicular to the Si substrate.[60] The anisotropy analysis of carbon samples will be discussed in detail elsewhere.[60]

It is now clear what the difference is between our magic-angle approach, giving ~85% sp^3 for a typical ta-C sample, and that of Koskinen, Hirvonen, and Keranen,[61] which gives a lower 66% sp^3 content. Their sp^3 fraction is lower due to a scattering geometry far from the magic-angle condition. They maximize the parallel momentum transfer for the reference sample, thus underestimating the sp^3 fraction.

We finally consider the integration intervals for sp^2 evaluation. Berger, McKenzie, and Martin[9] showed that the sp^2 fraction reached a stable value for an energy window greater than ~50 eV. On the other hand, Fallon[62] showed that with multiple scattering removal, the sp^3 content was stable after ~10 eV. Menon and Yuan[35] noted that the intensity at 311 eV does not change with convergence and collection angles. Moreover, for a typical plasmon energy of 30 eV, we expect the first significant contribution of multiple scattering around 310–315 eV. We thus suggest that the energy window should not extend to higher than 310–315 eV. Choosing the interval 281–289 eV for the π^* transition and 281–311 eV as normalizing window, the magic-angle graphite standard is 0.102.

The sp^3 contents measured at the magic angle are reported in Table I. Figure 9 shows that the sp^3 fraction slowly changes with ion energy for both the single-bend and S-bend FCVA. This differs from Fallon *et al.*[10] but agrees with the smoother variation found by others.[31,64] Thus the sp^3 fraction depends not only on ion energy, but also on other factors, such as deposition rate.[31]

E. EELS plasmon energy

The low-energy-loss spectrum in EELS is proportional to the energy-loss function, $\mathrm{Im}(-1/\varepsilon)$; ε is the complex dielectric function. In the free-electron limit, ε is given by the Drude model,[46]

$$\varepsilon(E)=1-\frac{E_p^2}{E^2+iE\Gamma} \tag{24}$$

so

$$\mathrm{Im}\left(-\frac{1}{\varepsilon(E)}\right)=\frac{E_p^2E\Gamma}{(E^2-E_p^2)^2+(E\Gamma)^2}, \tag{25}$$

where Γ is the full width at half maximum (FHWM) of the loss peak and E_p is the plasmon energy:

$$E_p=\hbar\left(\frac{n_e e^2}{\varepsilon_0 m^*}\right)^{1/2}, \tag{26}$$

where n_e is the valence electron density, ε_0 is the vacuum dielectric function, and m^* is the electron ''effective mass,'' m being the free-electron mass.

Our procedure is to measure the plasmon energy at the magic angle for the K edge. We will assess elsewhere the possible anisotropy effects on plasmon energy.[60]

In general, increasing the collection semiangle induces a shift in the plasmon energy, which increases slightly with the scattering vector **q**.[65] However, the q dispersion in a STEM for our experimental setup is expected to be small, due to the double integration between 0 and α and between 0 and β; see Fig. 6. In fact, the upwards shift can be ignored for $\beta<\theta_E^{0.5}=(E/2E_0)^{0.5}$, where E_0 is the incidence electron energy and θ_E is the characteristic angle.[46] $(E/2E_0)^{0.5}$ is ~12 mrad for 100 kV electrons and a typical 30 eV energy lost. We verified this by collecting low-loss spectra for a range of collection angles for a ta-C and an a-C sample. We detected only a very small up-shift at the magic angle of 7 mrad, within the experimental errors (<0.5 eV). Thus, since we are discussing a much larger density-change-driven plasmon shift on a relative coarse scale, we can neglect the plasmon energy shift due to the experimental setup.

The mass density is derived from the valence electron density n_e by assuming that carbon contributes four valence electrons, nitrogen five, and hydrogen one, to obtain

$$n_e = 12\frac{\rho N_A}{M_C}\left(\frac{3X_C+4X_N+1}{11X_C+13X_N+1}\right), \tag{27}$$

with $X_H = 1 - X_C - X_N$. Thus, the mass density is given by

$$\rho = \frac{\varepsilon_0}{12\hbar^2 N_A e^2} M_C m^* E_p^2 \frac{11X_C+13x_N+1}{3X_C+4X_N+1}. \tag{28}$$

Equations (11) and (28) for the mass density in XRR and EELS have a similar form. In Eq. (11) the unknown parameters are the critical angle θ_c, the carbon fraction X_C, and the nitrogen fraction X_N. In Eq. (28) the unknowns are plasmon energy, E_P, the carbon fraction X_C, the nitrogen fraction X_N, and the effective electron mass m^*. $4X_N$ in Eqs. (27) and (28) arises from the assumption of five valence electrons given by N. However, other groups propose to use three valence electrons,[66] giving $2X_N$ instead of $4X_N$ in Eq. (28).

The approximations in Eq. (28) are worse than those in Eq. (11). The weaker point of Eq. (28) is the unknown effective mass m^*, which arises from assuming a free-electron metal. So m^* has to include the effects of the neglected band gap (see later). Some groups empirically proposed to fit m^* so that the density of diamond (3.515 g/cm^3) corresponds to the observed plasmon energy, 33.8 eV.[10,32] This gives $m^* \sim 0.85m$. Other groups suggested to use $m^* = m$ and thus got $\sim$15% higher densities for the same plasmon energies.[34,4] Furthermore, Eq. (11) has a weaker dependence on H content than Eq. (24), so the XRR density is less affected by any error in the H content.

Let us consider approximations in Eq. (24) in more detail. First, Eq. (25) reaches a maximum at

$$E_{\max} \approx [E_P^2 - (\Gamma/2)^2]^{1/2}. \tag{29}$$

Some groups use $E_{\max}$ instead of E_P. This results in a systematic 5–10 % underestimation of the mass density, for typical values of E_P and Γ.

The major approximation is that diamond and amorphous carbons are semiconductors with a band gap E_G, while Eq. (24) implicitly assumes them as metals. The binding energy associated with E_G introduces a restoring force that changes the dielectric function as given by the Drude-Lorentz model,[12,1]

$$\varepsilon(E) = 1 + \frac{E_{P0}^2}{(E_G^2 - E^2 - iE\Gamma)}, \tag{30}$$

where E_{P0} is the *free-electron plasmon energy*. Thus the loss function is

$$\mathrm{Im}\left(-\frac{1}{\varepsilon(E)}\right) = \frac{E_{P0}^2 E\Gamma}{(E_G^2 + E_{P0}^2 - E^2)^2 + (E\Gamma)^2}. \tag{31}$$

Comparing Eqs. (25) and (31) we see that E_{P0} is lower than the observed plasmon energy E_P,

$$E_P^2 = E_{P0}^2 + E_G^2. \tag{32}$$

Here, E_G is the *Penn gap*, which is the average bonding-antibonding splitting, *not* the minimum gap.[67,68] E_G is 13.8 eV for diamond, compared to 5.5 eV for the minimum gap, and is quite large compared to $E_{P0} = 31$ eV.[68] For a typical

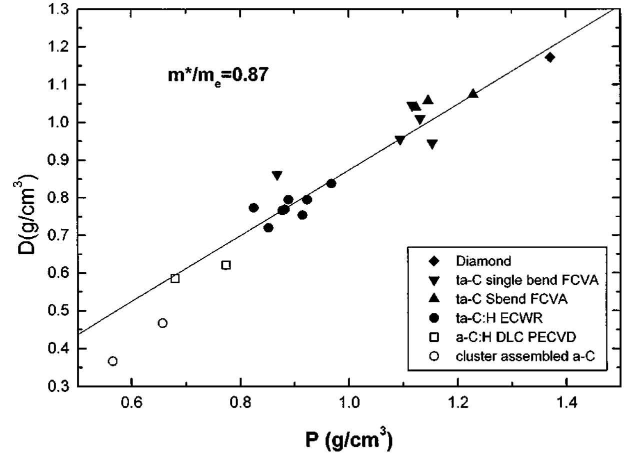

FIG. 10. Plot of $D = \rho_{\mathrm{XRR}}(3X_C+1)(11X_C+1)^{-1}$ against $P = M_c\varepsilon_0(12\hbar^2 N_A)^{-1}E_P^2$. D and P are the reduced densities of carbon films from XRR and EELS, respectively. The linear fit gives an average interband effective electron mass $m^* = 0.87m$.

ta-C we find $E_P \sim 30$ eV, $E_G \sim 11$ eV, and $E_{P0} \sim 27.8$ eV, while $E_{\mathrm{Tauc}} \sim 2.4$ eV. Since we take directly into account the interband transitions in E_G, the mass density has to be derived using Eq. (28) with m instead of m^* and E_{P0} instead of E_P. In fact, for diamond and a typical *ta*-C, E_{P0}^2 is $\sim$15% less than E_P^2. It is now clear why in the approach of Eqs. (24) and (25) one has to assume an effective electron mass $m^* \sim 0.85m$, while $m = m^*$ can only be used if E_{P0} is known. Thus, we formally define m^*, the *interband effective electron mass*, by the relation

$$\frac{m^*}{m} = \frac{E_{P0}^2}{E_P^2}. \tag{33}$$

How do we use this for amorphous carbons, where E_G and E_{P0} are not known *a priori*? In principle they could be derived by fitting Eqs. (25) and (31) to the same measured $\mathrm{Im}[-\varepsilon(E)^{-1}]$. However, an EELS measurement does not give the absolute $\mathrm{Im}[-\varepsilon(E)^{-1}]$, but $B\,\mathrm{Im}[-\varepsilon(E)^{-1}]$, where B depends on the precise experimental conditions, such as collection angle, beam energy, and specimen thickness, and cannot *a priori* be accounted for in a precise way (see Appendix). Thus, with B unknown, the two fits adjust to satisfy Eq. (32), without giving physically significant E_{P0} and E_G.

The concept of an interband effective mass is thus practically very useful when we want to get the density from EELS. As XRR gives the total electron density and EELS the valence electron density, we can directly fit an average m^* from our measured data on N free amorphous carbons. Figure 10 plots the reduced densities from XRR and EELS, $D = \rho_{\mathrm{XRR}}(3X_C+1)(11X_C+1)^{-1}$ against $P = M_C\varepsilon_0(12\hbar^2 N_A)^{-1}E_P^2$. If a unique m^* exists, then $D = (m^*/m)P$. We can fit data in Fig. 10 with a straight line of slope 0.87. This shows that the density can be derived from the plasmon energy for amorphous carbon films if we use $m^* = 0.87m$. Indeed, $m^* = 0.87m$ gives $E_P \sim 33.4$ eV for diamond, within the experimental error of the measured value. Figure 10 would suggest a common m^* holds for all amorphous carbons and diamond. From Eqs. (32) and (33) we get

$$\frac{E_G}{E_{P0}}=\left(\frac{m}{m^*}-1\right)^{1/2}, \quad \frac{E_G}{E_P}=\left(1-\frac{m^*}{m}\right)^{1/2}. \tag{34}$$

Thus, a constant m^* implies that the gap E_G is a constant fraction of the plasmon energy. This is reasonable and implies that a decrease of the plasmon energy is reflected in a decrease in the Penn gap, or, in other words, the gap decreases with decreasing sp^3 content.

There is an important corollary to the constant m^*. From Eq. (30), with $\varepsilon_2(0)\sim 0$ for *a*-C films, the dielectric constant and refractive index at zero energy are given by

$$[n(0)]^2=\varepsilon_1(0)=1+\frac{E_{P0}^2}{E_G^2}=\frac{E_P^2}{E_G^2} \tag{35}$$

or

$$[n(0)]^2=\varepsilon_1(0)=\left(1-\frac{m^*}{m}\right)^{-1}. \tag{36}$$

Thus, a constant $m^*=0.87m$ implies that the refractive index of amorphous carbons converges to the same value of 2.77 at $E=0$. This is indeed observed. For example Lifshitz *et al.*[69] and Chen and Zhao[70] found that n for *a*-C of different sp^3 content converges to $n(0)\sim 2.4-2.8$, with $n(0)=2.41$ for diamond. If the material becomes more graphitic, $k(0)$ is nonzero and so $n(0)$ will increase to give the same $\varepsilon(0)$.

We can rearrange Eq. (36) to give $m^*/m=1-[n(0)]^{-2}$, so from Eq. (35)

$$E_{P0}=\left[1-\frac{1}{[n(0)]^2}\right]^{1/2}E_P. \tag{37}$$

Thus, the zero-frequency refractive index $n(0)$ can be used as an experimental correction factor to the measured plasmon energy E_P, obtaining a more accurate density evaluation than using the fitted average m^*. In summary, the use of an interband effective mass m^* in Eq. (26) corrects for the presence of a covalent band gap on the loss function. This method includes in E_G also the effect of any correction factor used to allow for the effect of a finite Fermi energy in Eq. (35).[67,68]

Although $n(0)\sim 2.7$ holds reasonably well for hydrogen-free carbon, $n(0)$ falls to much lower values in polymeric *a*-C:H.[3,71] Typical values for a *a*-C:H with H>30% are $\varepsilon(0)\sim 3-4$ and $n(0)\sim 1.8-2.2$. This means that m^* for these *a*-C:H films is less than 0.87. Nevertheless, the density can be evaluated from Eq. (28) using the free-electron mass and E_{P0} derived from Eq. (37) using the experimental value of $n(0)$. To understand this, we have to consider the influence of H introduction on the Penn gap and electron density. Introducing H into *a*-C:H lowers the density and E_{P0}, but raises the minimum optical gap (because it removes the π-π^* transitions). Moreover, C-H σ-σ^* transitions lie at similar energies to C-C σ-σ^* transitions, so the Penn gap does not decrease with H introduction and is no longer a constant fraction of E_{P0}. Indeed E_G/E_{P0} increases with H, thus $n(0)$ declines and m^* will decrease in *a*-C:H. Thus, the fall in density of *a*-C:H with increasing H content is not reflected in a proportional decrease of E_P. Plasmon energies will overestimate the density using the average m^*.

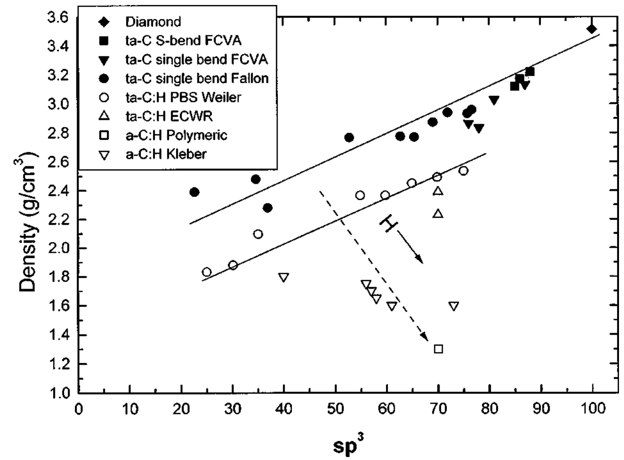

FIG. 11. Correlation of the density and sp^3 fraction for *ta*-C and *ta*-C:H films, showing a near-linear dependence for the two classes of films. We plot also the density of the polymeric *a*-C:H and of a series of *a*-C:H with increasing H content [after Kleber *et al.* (Ref. 72)]. The dashed line indicates the trend of decreasing density with increasing sp^3 and H content for *a*-C:H.

Indeed, in *a*-C:H E_P is never lower than 22–23 eV, but XRR gave densities as low as 1.2 g/cm^3. From the measured $n(0)$ we can estimate the minimum m^* for polymeric *a*-C:H to be ~0.7 m.

On the other hand, Fig. 10 shows that the fitted m^* reproduces well the densities of *ta*-C:H and of the graphitic *a*-C:H. This again implies that the corrections on m^* will become important only for high-H-content polymeric *a*-C:H.

We now consider the relationship between density and sp^3 fraction. Figure 11 shows the correlation of sp^3 content to density for *ta*-C and *ta*-C:H films using our data, those of Weiler *et al.*[40] and Fallon *et al.*,[10] scaled with our fitted m^*. The H content of *ta*-C:H is almost constant, ~25–30 at. %. Note that there is no common sp^3 density relationship for *ta*-C and *ta*-C:H differently from that proposed by Weiler *et al.*[40] *ta*-C:H densities reported by Weiler *et al.* are 15% overestimated due to the use of $m=m^*$.[40] Our data from XRR on similar *ta*-C:H films indicate a maximum density of 2.35 g/cm^3, comparable with the ~2.4 g/cm^3 obtained scaling the original data of Weiler *et al.*[40]

A linear fit of the H-free data gives

$$\rho \ \ (\text{g/cm}^3)=1.92+1.37(sp^3 \text{ fraction}). \tag{38}$$

Equation (38) gives a density of ~3.3 g/cm^3 for 100% sp^3 content, lower than diamond, but consistent with a random distribution of sp^3 sites. The increase of density and sp^3 fraction for a fixed H content is the main difference between *ta*-C:H and *a*-C:H, where the increase in sp^3 fraction is obtained through an increase in H content and thus a decrease in the density. *ta*-C:H with higher H content results in lines parallel to that in Fig. 11. On the other hand, a series of *a*-C:H films with increasing H content will result in a line with an opposite slope with respect to *ta*-C or *ta*-C:H, as schematically shown by the dashed line in Fig. 11.

For *ta*-C:H:N and *ta*-C:N samples a good agreement with XRR was obtained using the fitted m^* and five valence electrons, confirming in this case the factor $4X_N$ in Eq. (28). However, a systematic study on samples with different N

content, N hybridization and C sp^3 content is necessary to confirm this. In fact, for Si_3N_4 the density could be derived from plasmon energy assuming totally free electrons and three valence electrons for N.[66]

IV. CONCLUSIONS

A wide variety of amorphous carbon films have been analyzed via XRR and EELS. XRR is shown to be the method of choice to measure their density and cross-sectional structure even for ultrathin films in the nanometer range. We gave a formal definition of the interband effective electron mass m^*. Comparing XRR and EELS data we could fit a common average m^* for all amorphous carbon films and diamond, validating the jellium approach to the density from plasmon energy. We have thus shown the consistent general relationship between sp^3 and mass density for *ta*-C and *ta*-C:H.

The cross-sectional structure of hydrogenated films is found to be quite uniform, with less than 1–2 nm interface and surface layers. *ta*-C can possess a heavy layering depending on the deposition conditions. However, layering is not intrinsic, but it is due to plasma instabilities in the arc, and uniform films can be grown. Our S-bend FCVA is found to give the most uniform *ta*-C films. Plasmon energy is convenient to get the average density of heavily layered films when fitting of XRR data is difficult. We have refined the method for calculating the sp^2 content from the EELS carbon *K* edge, in order to make it independent of anisotropy effects.

ACKNOWLEDGMENTS

The authors thank M. C. Polo, N. A. Morrison, N. Conway, J. Seekamp, X. L. Peng, P. Milani, P. M. Ossi, and K. B. K. Teo for some of the samples used in this study; E. Riedo for plasmon energy of cluster assembled *a*-C; J. Fink and V. Paret for discussions on dielectric functions. A.C.F. and B.K. acknowledge E. U. Marie Curie funding. A. L. acknowledges support from the Italian INFM and MURII/British Council exchange grant.

APPENDIX

In principle, the better way to get E_G is to perform Kramers-Kronig[1,46,73] (KK) analysis of the low loss and then fit E_G from $\varepsilon_2(E)=\mathrm{Im}[\varepsilon(E)]$. However, an EELS measurement does not give the absolute $\mathrm{Im}[-\varepsilon(E)^{-1}]$, but $B\,\mathrm{Im}[-\varepsilon(E)^{-1}]$, where B depends on the precise experimental conditions, as stated in Sec. III E. In practice the KK method is not very simple, due to the zero-loss removal and necessity of boundary conditions and sum rules for analysis. The sum rules ultimately set B, which, if known, allows a direct determination of E_G from the low-loss spectrum. Nevertheless, it is convenient to express m^* as a function of integral quantities, which could be less sensitive to extrapolations or measurement errors than $\varepsilon(0)$ and $n(0)$. We thus consider the jth moment of the imaginary part of the dielectric function, $\varepsilon_2(E)$:[74]

$$M_j(\varepsilon_2)=\int_0^\infty \varepsilon_2(E)E^j dE. \tag{A1}$$

From the KK relationships and the sum rules of the dielectric function we have[74]

$$E_G^2=\frac{M_1(\varepsilon_2)}{M_{-1}(\varepsilon_2)}, \tag{A2}$$

with

$$M_1(\varepsilon_2)=M_1[\mathrm{Im}(-1/\varepsilon)]=\frac{\pi E_{P0}^2}{2}. \tag{A3}$$

From Eqs. (33) and (34) m^* is thus given by

$$\frac{m^*}{m}=1-\left[1-\frac{2M_{-1}(\varepsilon_2)}{\pi}\right]^{-1}. \tag{A4}$$

Alternatively, from $\mathrm{Im}(-1/\varepsilon)$ and the KK relations,[1] we get

$$\frac{E_G^2}{E_P^2}=1-\frac{2}{\pi}M_{-1}\left[\mathrm{Im}\left(\frac{-1}{\varepsilon}\right)\right], \tag{A5}$$

which gives

$$\frac{m^*}{m}=\frac{2}{\pi}M_{-1}\left[\mathrm{Im}\left(\frac{-1}{\varepsilon}\right)\right]. \tag{A6}$$

Note that Eqs. (A4)–(A6) do not give any more information than Eq. (36) if ε is derived by a KK analysis from low-loss data. In fact, when doing KK analyses one has to fix B.[73] This is usually done fixing the refractive index at low energy, but as discussed in Sec. III E, once we know $n(0)$ and the plasmon energy, we can directly get E_G and m^*. However ε can be directly obtained by other optical measurements,[71] and thus integral relations such as Eqs. (A4)–(A6) become more useful. More interestingly, a measure of total electron density with XRR and of E_P with EELS can be used to derive m^*. This gives an alternative way to set the sum rules for the KK analysis. This also allows for an independent check for optical measurements at low energy. Furthermore, fulfilling sum rules on M_{-1} is more convenient than on M_1, due to the limited E range in high-resolution EELS measurements or optical measurements.

*Email address: acf26@eng.cam.ac.uk

[1] J. Fink, in *Advances in Electronics and Electron Physics*, edited by P. W. Hawkes (Academic, New York, 1989) Vol. 75, p. 122.

[2] T. Pichler, M. Knupfer, M. S. Golden, S. Haffner, R. Friedlein, J. Fink, W. Andreoni, A. Curioni, M. Keshavarz-k, C. Bellavia-Lund, A. Sastre, J. Hummelen, and F. Wuld, Phys. Rev. Lett. **78**, 4249 (1997); T. Pichler, M. Knupfer, M. S. Golden, J. Fink, A. Rinzler, and R. E. Smalley, *ibid.* **80**, 4729 (1998).

[3] J. Fink, T. Muller-Heinzerling, J. Pfluger, A. Bubenzer, P. Koidl, and G. Cercelius, Solid State Commun. **47**, 687 (1983); J. Fink, Th. Muller-Heinzerling, J. Pfluger, B. Scheerer, B. Dishler, P. Koidl, A. Bubenzer, and R. E. Sah, Phys. Rev. B **30**, 4713 (1984).

[4] J. J. Cuomo, J. P. Doyle, J. Bruley, and J. C. Liu, Appl. Phys.

Lett. **58**, 466 (1991).

[5] R. H. Jarman, G. J. Ray, R. W. Stanley, and G. J. Zajac, Appl. Phys. Lett. **49**, 1065 (1986).

[6] J. Kulik, Y. Lifshitz, G. D. Lempert, J. W. Rabalais, and D. Marton, J. Appl. Phys. **76**, 5063 (1994).

[7] V. I. Merkulov, D. H. Lowndes, G. E. Jellison, A. A. Puretzky, and D. B. Geohegan, Appl. Phys. Lett. **73**, 2591 (1999).

[8] P. J. Fallon and L. M. Brown, Diamond Relat. Mater. **2**, 1004 (1993).

[9] S. D. Berger, D. R. McKenzie, and P. J. Martin, Philos. Mag. Lett. **57**, 285 (1988).

[10] P. J. Fallon, V. S. Veerasamy, C. A. Davis, J. Robertson, G. A. J. Amaratunga, and W. I. Milne, Phys. Rev. B **48**, 4777 (1993); **49**, 2287(E) (1993).

[11] C. A. Davis, K. M. Knowles, and G. A. J. Amaratunga, Surf. Coat. Technol. **76-77**, 316 (1995); Phys. Rev. Lett. **80**, 3280 (1998).

[12] H. Raether, *Excitation of Plasmons and Interband Transitions by Electrons*, Springer Tracts in Modern Physics (Springer, New York, 1980), Vol. 38.

[13] L. G. Parrat, Phys. Rev. **95**, 359 (1954).

[14] B. Lengeler, in *X-Ray Absorption and Reflection in the Hard X-Ray Range*, edited by M. Campagna and K. Rosei (North-Holland, Amsterdam, 1990).

[15] M. Wormington, I. Pape, T. P. A. Hase, B. K. Tanner, and D. K. Bowen, Philos. Mag. Lett. **74**, 211 (1996).

[16] S. K. Sinha, E. N. Sirota, and S. Garoff, Phys. Rev. B **38**, 2297 (1988).

[17] M. Wormington, C. Panaccione, K. M. Matney, and D. K. Bowen, Philos. Trans. R. Soc. London, Ser. A **357**, 2827 (1999).

[18] I. Pape, B. K. Tanner, and M. Wormington, J. Non-Cryst. Solids **248**, 75 (1999).

[19] A. Libassi, A. C. Ferrari, V. Stolojan, B. K. Tanner, J. Robertson, and L. M. Brown, Diamond Relat. Mater. **9**, 771 (2000).

[20] E. Kondrashov, I. S. Smirnov, E. G. Novoselova, S. Yu. Yablokov, and A. M. Baranov, Diamond Relat. Mater. **6**, 1784 (1997).

[21] S. Logothetidis and G. Stergioudis, Appl. Phys. Lett. **71**, 2463 (1997).

[22] A. Lucas, T. D. Nguyen, and J. B. Kortright, Appl. Phys. Lett. **59**, 2100 (1991).

[23] M. J. Grundy, R. M. Richardson, J. Roser, G. Beamson, W. J. Brennan, J. Howard, M. O'Neil, J. Penfold, C. Shackleton, and C. Ward, Thin Solid Films **172**, 269 (1989).

[24] E. Findeisen, R. Feidenhans'l, M. E. Vigild, K. N. Clausen, J. Bindslev Hansen, M. D. Bentzon, and J. P. Goff, J. Appl. Phys. **76**, 4636 (1994).

[25] F. Toney and S. Brennan, J. Appl. Phys. **66**, 1861 (1989).

[26] Y. Huai, M. Chaker, J. N. Broughton, E. Gat, H. Pepin, T. Gu, X. Bian, and M. Sutton, Appl. Phys. Lett. **65**, 830 (1994).

[27] Q. Zhang, S. F. Yoon, Rusli, J. Ahn, H. Yang, and D. Bahr, J. Appl. Phys. **84**, 5538 (1998); **86**, 289 (1999).

[28] J. Martinez-Miranda, J. P. Sullivan, T. A. Friedmann, M. P. Siegal, and N. J. DiNardo, in *Covalently Bonded Thin Film Materials*, edited by M. P. Siegal *et al.*, MRS Symposia Proceedings No. 498 (Materials Research Society, Pittsburgh, 1998), p. 55.

[29] M. P. Siegal, J. C. Barbour, P. N. Provencio, D. R. Tallant, and T. A. Friedmann, Appl. Phys. Lett. **73**, 759 (1998); M. P. Siegal, D. R. Tallant, L. J. Martinez-Miranda, J. C. Barbour, R. L. Simpson, and D. L. Overmyer, Phys. Rev. B **61**, 10 451 (2000); M. P. Siegal, P. N. Provencio, D. R. Tallant, R. L. Simpson, B. Kleinsorge, and W. I. Milne, Appl. Phys. Lett. **76**, 2047 (2000).

[30] J. Robertson, in *Diamond and Diamond-like Carbon*, edited by R. E. Clausing *et al.*, NATO ASI Publication No. B266 (Plenum, New York, 1991), p. 331.

[31] Y. Lifshitz, Diamond Relat. Mater. **8**, 1659 (1999).

[32] D. R. McKenzie, D. Muller, and B. A. Pailthorpe, Phys. Rev. Lett. **67**, 773 (1991).

[33] J. Schwan, S. Ulrich, T. Theel, H. Roth, H. Ehrhardt, P. Beker, and S. R. P. Silva, J. Appl. Phys. **82**, 6024 (1997).

[34] D. G. McCulloch, E. G. Gernstner, D. R. McKenzie, S. Prawer, and R. Kalish, Phys. Rev. B **52**, 850 (1995).

[35] N. K. Menon and J. Yuan, Ultramicroscopy **74**, 83 (1998); **78**, 185 (1999); N. K. Menon, Ph.D. thesis, Cambridge University (1998).

[36] V. Stolojan, L. M. Brown, A. C. Ferrari, J. Robertson, A. LiBassi, and B. K. Tanner, in Proceedings of the Electron Microscopy and Analysis Group Conference, Sheffield 1999, IOP Conf. Proc. No. 161 (Institute of Physics, London, 1999), p. 361.

[37] M. C. Polo, J. L. Andujar, A. Hart, J. Robertson, and W. I. Milne, Diamond Relat. Mater. **9**, 663 (2000).

[38] M. Bonelli, A. C. Ferrari, A. P. Fioravanti, A. Miotello, and P. M. Ossi, in *Amorphous and Nanostructured Carbon*, edited by J. P. Sullivan, J. Robertson, O. Zhou, T. B. Allen, and B. F. Coll, MRS Symposia Proceedings No. 593 (Materials Research Society, Pittsburgh, 2000), p. 359.

[39] N. A. Morrison, S. E. Rodil, A. C. Ferrari, J. Robertson, and W. I. Milne, Thin Solid Films **337**, 71 (1999).

[40] M. Weiler, S. Sattel, T. Giessen, K. Jung, H. Ehrhardt, V. S. Veerasamy, and J. Robertson, Phys. Rev. B **53**, 1594 (1996); M. Weiler *et al.*, Diamond Relat. Mater. **3**, 245 (1994); M. Weiler, Ph.D. thesis, Universitat Kaiserslautern (1994).

[41] S. E. Rodil, N. A. Morrison, J. Robertson, and W. I. Milne, Phys. Status Solidi A **174**, 25 (1999).

[42] S. E. Rodil, W. I. Milne, J. Robertson, and L. M. Brown, Appl. Phys. Lett. **77**, 1458 (2000).

[43] X. L. Peng and T. W. Clyne, Thin Solid Films **312**, 207 (1998).

[44] E. Barborini, P. Piseri, A. Libassi, A. C. Ferrari, C. E. Bottani, and P. Milani, Chem. Phys. Lett. **300**, 633 (1999).

[45] D. E. Savage, J. Kleiner, N. Schimke, Y. H. Phang, T. Jankowsky, J. Jacobs, R. Kariotis, and M. G. Legally, J. Appl. Phys. **69**, 1411 (1991); D. E. Savage, N. Schimke, Y. H. Pang, and M. G. Legally, *ibid.* **71**, 3283 (1992).

[46] R. F. Egerton, *Electron Energy Loss Spectroscopy in the Electron Microscope* (Plenum, New York, 1986).

[47] http://www-cxro.1bl.gov/optical constants/

[48] G. H. Vineyard, Phys. Rev. B **26**, 4146 (1982).

[49] R. J. Rigden, R. J. Newport, and G. Bushnell-Wye, J. Mater. Res. **12**, 264 (1997).

[50] A. C. Ferrari, J. Robertson, M. G. Beghi, C. E. Bottani, R. Ferulano, and R. Pastorelli, Appl. Phys. Lett. **75**, 1893 (1999).

[51] Y. Lifshitz, S. R. Kasi, J. W. Rabalais, and W. Eckstein, Phys. Rev. B **41**, 10 468 (1990).

[52] J. Robertson, Diamond Relat. Mater. **2**, 984 (1993).

[53] I. G. Brown, Annu. Rev. Mater. Sci. **28**, 243 (1998).

[54] D. R. McKenzie, E. G. Gernstner, D. G. McCulloch, and C. M. Goringe, in *Amorphous Carbon: State of the Art*, edited by S. R. P. Silva *et al.* (Word Scientific, Singapore, 1998), p. 3.

[55] A. J. Craven, T. W. Buggy, and R. P. Ferrier, in *Quantitative Microanalysis with High Spatial Resolution*, edited by G. M. Lorimer *et al.* (The Metals Society, London, 1981), p. 141.

[56] H. Kohl, Ultramicroscopy **16**, 265 (1985).

[57] N. D. Browning, J. Yuan, and L. M. Brown, Ultramicroscopy **38**, 291 (1991).
[58] I. Alexandrou, H. J. Scheibe, C. J. Kiely, A. J. Papworth, G. A. J. Amaratunga, and B. Schultrich, Phys. Rev. B **60**, 10 903 (1999).
[59] J. Yuan, in Proceedings of the ICEM14, IOP Proc. No. III (Institute of Physics, Bristol, 1998); J. Yuan and L. M. Brown, Micron. **31**, 515 (2000).
[60] V. Stolojan, A. C. Ferrari, J. Yuan, L. M. Brown, and J. Robertson (unpublished).
[61] J. Koskinen, J. P. Hirvonen, and J. Keranen, in *Amorphous Carbon: State of the Art*, edited by S. R. P. Silva *et al.* (World Scientific, Singapore, 1998), p. 46.
[62] P. J. Fallon, Ph.D. thesis, Cambridge University (1992).
[63] M. Chhowalla, Ph.D. thesis, Cambridge University (1998).
[64] B. K. Tay, X. Shi, L. K. Cheah, and D. I. Flynn, Thin Solid Films **308**, 199 (1997).
[65] P. E. Batson and J. Silcox, Phys. Rev. B **27**, 5224 (1983).
[66] E. B. Halac, H. Huck, G. Zampieri, R. G. Pergliasco, E. Alonso, and M. A. R. de Benycar, Appl. Surf. Sci. **120**, 139 (1997).
[67] D. R. Penn, Phys. Rev. **128**, 2093 (1962).
[68] J. C. Phillips, *Bonds and Bands in Semiconductors* (Academic, New York, 1973).
[69] Y. Lifshitz *et al.*, Diamond Relat. Mater. **6**, 687 (1997).
[70] Z. Y. Chen and J. P. Zhao, J. Appl. Phys. **87**, 4268 (2000).
[71] V. Paret *et al.*, J. Non-Cryst. Solids **227**, 583 (1998); V. Paret, These de Doctorat, Université Paris VI (1999).
[72] R. Kleber, K. Jung, H. Ehrhardt, I. Muhling, K. Breuer, H. Metz, and F. Engelke, Thin Solid Films **205**, 274 (1991).
[73] S. Waidmann, M. Knupfer, J. Fink, B. Kleinsorge, and J. Robertson, Diamond Relat. Mater. **9**, 722 (2000).
[74] J. J. Hopfield, Phys. Rev. B **2**, 973 (1970).